scientific reports

OPEN

Single step nanosecond laser structuring for cost effective functional titanium surfaces with topography driven preosteoblast adhesion

Adriana Barylyak[1], Sarunas Meskinis[2], Algirdas Lazauskas[2], Piotr Krzemiński[3], Renata Wojnarowska-Nowak[3], Małgorzata Trzyna-Sowa[3], Marta Trzaskowska[4], Vladyslav Vivcharenko[4], Bogumił Cieniek[3], Agata Przekora[4], Andrzej Dziedzic[3], Yaroslav Bobitski[3] & Joanna Kisała[3]✉

Early bone formation around implants depends on both the chemical composition and the micro-, nanoscale architecture of the implant surface. Nanoscale modifications can accelerate osseointegration, and laser processing offers a versatile method of creating such features. In this study, titanium substrates were modified using a single-step nanosecond laser treatment at two energy regimes (1.95 mJ/pulse for P_0.5; 4.00 mJ/pulse for P_0.4). The resulting surfaces were characterized by SEM, EDS, XRD, Raman spectroscopy, ToF-SIMS, contact angle, and topography measurements, with biological assessment performed using a mouse preosteoblast cell line. Analyses revealed various titanium oxo clusters (TiO_3^-, TiO_2^-, TiO^-) and moderate oxidation levels (25–31 at% O). Both laser regimes produced rough, hydrophobic surfaces. Cytotoxicity tests confirmed that the materials were non-toxic, and proliferation assays showed increasing preosteoblast numbers over time, indicating that both surfaces supported cell division. Good adhesion of preosteoblasts was observed on P_0.4 and P_0.5. This work demonstrates that nanosecond laser processing alone can generate micro-, nanostructured titanium implant surfaces with favourable biocompatibility, achieving performance comparable to more complex femtosecond methods while offering a cost-effective and scalable surface engineering strategy.

Keywords Laser surface modification, Nanosecond laser, Biocompatibility, Cell adhesion, Roughness, Wettability

Titanium and its alloys are widely used for load-bearing implants due to their good tissue tolerance and ability to support robust osseointegration[1,2]. However, long-term clinical success is not always achieved; early implant failure from insufficient osseointegration occurs in about 1–2% of cases, with late failure rates around 5%. Implant osseointegration involves an initial mechanical anchorage (primary stability) that transitions to a biological bond (secondary stability), during which a transient decrease in stability may be observed. Enhancing implant material performance remains critical due to growing clinical demand. Successful osseointegration depends on balancing bone resorption and formation during remodelling, which is influenced by the implant surface's micro- and nanoscale topography and chemistry[3,4]. The micro- and nanoscale topographical characteristic, as well as the chemical composition, of the implant surfaces are fundamental determinants of initial bone formation at the implant-bone interface[5,6]. Engineered nanoscale features enhance protein adsorption and promote osteoblast attachment, thereby facilitating and accelerating osseointegration process[7–9]. Laser surface treatment offers

[1]Danylo Halytsky Lviv National Medical University, Pekarska Str. 69, Lviv 79010, Ukraine. [2]Institute of Materials Science, Kaunas University of Technology, K. Baršausko 59, 51423 Kaunas, Lithuania. [3]Faculty of Exact and Technical Sciences, University of Rzeszow, Pigonia 1 Str., Rzeszow 35-310, Poland. [4]Department of Tissue Engineering and Regenerative Medicine, Medical University of Lublin, Chodzki 1 Str., 20-093 Lublin, Poland. ✉email: jkisala@ur.edu.pl

precise, reproducible modification of surface morphology while minimizing processing time and cost[10–13]. By adjusting laser parameters, surface characteristics can be tuned without altering bulk properties.

Both femtosecond (fs) and nanosecond (ns) lasers enable precise control over surface roughness, topography, and chemical composition, which are critical for regulating cell adhesion, proliferation, and differentiation. Femtosecond lasers can create well-defined microgrooves, ripples (LIPSS), and hierarchical textures with minimal thermal damage, enabling precise control over cell orientation and migration. These structures promote osteoblast adhesion and differentiation, often outperforming polished[14,15].

Nanosecond laser-ablated titanium alloys often show high surface free energy, and at a given chemistry, moderate roughness on such surfaces is beneficial for cell adhesion[16]. Nanosecond laser-textured Ti and Ti alloys generally exhibit increased osteoblast or mesenchymal stem cells adhesion on appropriately rough, high-energy surfaces, and several studies report promoted proliferation and osteogenic differentiation relative to machined or polished references, although responses may plateau or decline if roughness or melt-recast is excessive[17]. Direct comparisons suggest nanosecond laser-treated surfaces can give stronger early attachment but lower cell numbers or different differentiation profiles than femtosecond laser-treated ones. Achieving consistent results across different batches and implant geometries is difficult due to variations in laser parameters, material properties, and processing conditions[18]. Standardization of protocols is essential for reliable clinical translation. Addressing the issues in crack formation, consistency, long-term stability, and large-scale manufacturing is essential for translating these advances into clinical practice.

Traditionally, optimal titanium implant surfaces have been engineered toward maximum oxidation and superhydrophilicity - typically achieved only with complex, high-cost femtosecond lasers - to promote protein adsorption and osteoblast adhesion. This work overturns that dogma by demonstrating that a single-step nanosecond laser process, producing only moderate oxidation (25–31 at% O) and hydrophobic surfaces (contact angles > 90°), can achieve equivalent preosteoblast adhesion and proliferation. This finding represents a fundamental re-evaluation of the relationship between surface properties and biological efficacy, demonstrating that achieving optimal cellular response is not mandatorily dependent on maximal surface oxidation or inherent superhydrophilicity.

Materials and methods

Materials

The material utilized in this study comprised grade 4 titanium disc samples, which represent the most commonly employed titanium grade for dental implants, and conformed to the ASTM B348 and EN10204/3.1 standards.

Surface preparation

Titanium rod was sectioned into discs measuring 6 mm in diameter and 2 mm in height, followed by mirror polishing to achieve flat surfaces suitable for laser treatment. Laser processing was conducted in an ambient air atmosphere using an Nd: YAG fiber laser (Shandong Reaying Machinery Co., Ltd., Jinan, China) operated at 30% of its nominal 30 W power output, with a wavelength of 1064 nm. The laser emitted pulses with a full width at half maximum duration of approximately 120 ns, at a repetition rate of 70 kHz, and a scanning speed of 7000 mm/s. The laser spot size was approximately 20 µm, and the line spacing during scanning was set to either 40 µm (P_0.4) or 50 µm (P_0.5.). The laser parameters are summarized in Table 1.

Physicochemical, morphological and microstructural surfaces characterisation

Surface morphology images of the prepared samples were obtained using a Helios NanoLab 650 field emission scanning electron microscope (FESEM) (FEI, Hillsboro, Oregon, USA). The instrument was operated at accelerating voltages of 5 kV and 30 kV, employing an Everhart-Thornley detector (ETD) for secondary electron imaging (SE mode). Additionally, elemental composition analysis was performed via Energy-Dispersive X-ray Spectroscopy (EDS) using an EDAX detector (AMETEK, Berwyn, PA, USA). The analyses encompassed the full surface area of each sample. The analysis of crystalline structure of surfaces was conducted by an X-ray diffractometer (XRD) (D8 Advance, Bruker, Germany) with 0.15406 nm Cu K_α radiation.

Surface roughness was measured using Olympus OLS5100 LEXT 3D confocal laser microscope (Olympus Co., Tokio, Japan). The samples were analysed at a magnification of 421×. Ten different areas of each sample were examined, and 5 measurements of roughness profile were taken for each area.

Raman spectra were acquired using an *inVia* Micro Raman spectrometer (Renishaw, Wotton under Edge, Gloucestershire, UK) coupled with a Leica DM 2500 M microscope (Leica Microsystems GmbH, Wetzlar, Germany), employing a 633 nm laser for excitation. Measurements were conducted in both spot metering and mapping modes.

The wettability study was conducted using a DSA 30 goniometer. Contact angle measurements were made by depositing an ultrapure water droplet on the biomaterial surface. Eight measurements were taken for each sample.

Sample	Energy per pulse, Ep (mJ)	Repetition rate, RR (kHz)	Step, (µm)	Scanning speed, Vs (m/s)	Pulse duration, τ (ns)	Polarisation
P_0.4	4.00	70	40	7	120	⊥
P_0.5	1.95	70	50	7	120	⊥

Table 1. Laser process parameters.

Time-of-Flight Secondary Ion Mass Spectrometry (ToF-SIMS) analyses were performed using a TOF SIMS V spectrometer (ION TOF GmbH) under ultra-high vacuum conditions ($\sim 1 \times 10^{-10}$ mbar). ToF-SIMS analysis was used for qualitative identification of oxide clusters and assessment of their distribution over the studied surfaces. Data acquisition and processing utilized SurfaceLab 6.8 software. Positive and negative ion mass spectra were collected from 500 µm × 500 µm sample areas using a pulsed 30 keV Bi^+ primary ion source at a current of 1.27 pA over 500 scans, ensuring a total fluence of less than 5×10^{12} Bi^{3+} ions/cm^2 under static mode. Depth profiling was conducted in dual-beam mode; the analysis beam consisted of a rastered pulsed 30 keV Bi^+ ion source (1.27 pA) over a 100 µm × 100 µm area, while sputtering employed a 2 keV, 80 nA Cs^+ ion beam rastered over 300 µm × 300 µm. Both beams impinged on the sample surface at 45° relative to the surface normal. Corresponding mass spectra and depth profiles are detailed in the Supplementary Material.

Surface photocatalytic properties

Photocatalytic activity was evaluated by monitoring the degradation of methylene blue (MB). Titanium discs (K, P_0.4, P_0.5) were immersed in MB solution (4 cm^3, 5×10^{-5} mol dm^{-3}, pH = 6) in a quartz cuvette. An MB solution without discs was irradiated under identical conditions to assess photolysis. Illumination was provided by a custom blue diode lamp (455 nm, 8.78 W m^{-2}, Peak Tech 5025 m) positioned 30 cm from the sample. MB degradation was quantified spectrophotometrically (VWR UV-VIS 3100 PC) at regular intervals using calibration standards ($5 \times 10^{-5} - 5 \times 10^{-6}$ mol dm^{-3}).

Evaluation of material biocompatibility

Mouse calvaria-derived preosteoblasts (MC3T3-E1 Subclone 4, ATCC) were utilized for cell culture experiments. Cells were maintained in Alpha Minimum Essential Medium (αMEM; GIBCO, Life Technologies, NY, USA) supplemented with 10% fetal bovine serum (FBS; Pan Biotech GmbH) and antibiotics comprising 0.1 mg/mL streptomycin and 100 U/mL penicillin (Sigma-Aldrich Chemicals, MO, USA). Cultures were incubated at 37 °C in a humidified atmosphere containing 5% CO_2 in air.

Cytotoxicity test

The cytotoxicity assessment was conducted using a direct-contact approach with the biomaterial samples. Specimens were placed in 24-well plates and preincubated in complete culture medium for one hour prior to cell seeding. MC3T3-E1 cells were then directly seeded onto the biomaterial surfaces at a density of 4×10^4 cells per sample and cultured for 48 h. Tissue culture-treated coverslips (Thermanox Plastic Coverslips, Thermo Scientific Nunc, NY, USA) were used as the control substrate. Following the incubation period, cell viability was evaluated by measuring lactate dehydrogenase (LDH) release according to the manufacturer's protocol (Roche Diagnostics, Warsaw, Poland).

Additionally, cytotoxic effects were assessed qualitatively via Live/Dead fluorescent staining followed by confocal laser scanning microscopy (CLSM) analysis (Olympus Fluoview FV1000, Olympus Polska Sp. z o.o., Warsaw, Poland). Cultures were prepared analogously, with cells seeded at 4×10^4 per sample and incubated for 48 h, then stained using the Live/Dead Double Staining Kit (Sigma-Aldrich Chemical, Warsaw, Poland) per the manufacturer's instructions before imaging.

Proliferation assay

Cell proliferation was evaluated through direct contact with the biomaterial samples, prepared as described in the Cytotoxicity Test section. MC3T3-E1 cells were seeded onto the material surfaces at a density of 1×10^3 cells per sample and cultured for 24, 48, and 96 h. Tissue culture-treated coverslips served as the control. The increase in cell number over time was quantified using the colorimetric Cell Counting Kit-8 (WST-8 assay; Sigma-Aldrich Chemicals) following the manufacturer's protocol. Cell numbers were calculated based on a calibration curve generated from known cell concentrations.

Additionally, cytoskeletal organization was examined at each time point (24, 48, and 96 h) using confocal laser scanning microscopy (CLSM). Cells were fixed with paraformaldehyde, permeabilized with Triton-X, and stained for actin filaments using Alexa Fluor 635-conjugated phalloidin (Invitrogen, Carlsbad, CA, USA), while nuclei were counterstained with DAPI (Sigma-Aldrich Chemicals, Warsaw, Poland).

Statistical analysis

The results of all assays were expressed as mean values ± standard deviation (SD). Each experiment was performed in at least three independent repetitions. In each assay, all samples were tested in three independent technical replicates. Statistical significance in the cytotoxicity assay between control cells and those cultured on the test biomaterials was determined using one-way analysis of variance (ANOVA) followed by Dunnett's post-hoc test, with significance defined at $p \leq 0.05$. For the proliferation assay, differences among groups were analyzed by one-way ANOVA with Tukey's multiple comparisons test, considering $p \leq 0.05$ as statistically significant. All statistical analyses were performed using GraphPad Prism software version 8.0.0 (GraphPad Software Inc[19].

Results and discussion

Characterisation of surfaces

The influence of laser processing power on the microstructure and surface morphology of titanium specimens was examined by scanning electron microscopy (SEM). Laser structuring led to obtaining a surface with quite uniform morphology in the case of sample P_0.4, whereas the pattern of grooves can be observed for sample P_0.5 (Fig. 1a, d).

The distance between the bands of the laser beam on the titanium surface in sample P_0.5 is ca. 50 µm. During laser irradiation, a superposition of ablation and surface melting processes is apparently observed. As

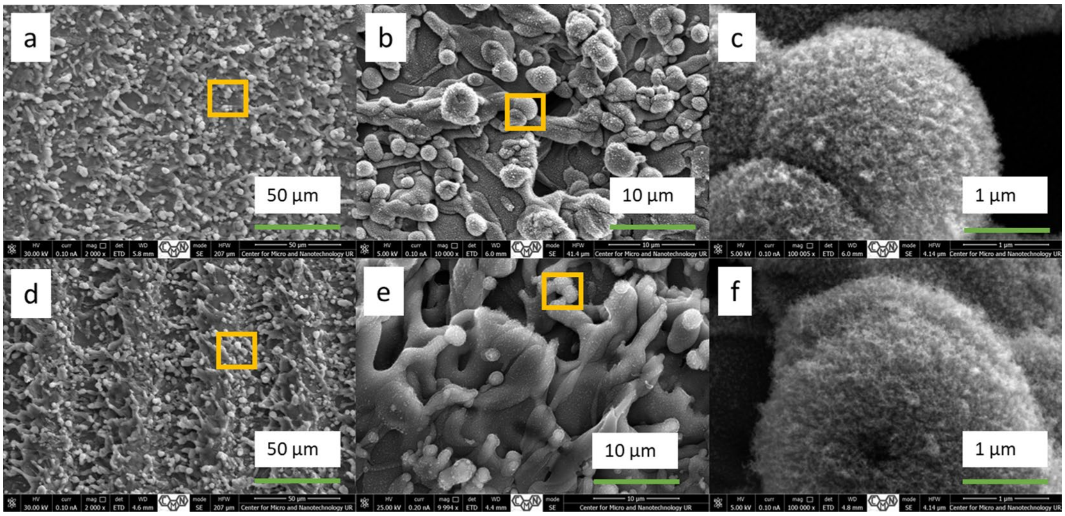

Fig. 1. SEM images of samples P_0.4 in 2000 x magnification (a); P_0.4 in 10 000 x magnification (b); P_0.4 in 100 000 x magnification (c); P_0.5 in 2000 x magnification (d); P_0.5 in 10 000 x magnification (e); P_0.5 in 100 000 x magnification (f).The crystalline phases were characterised by XRD diffraction measurements using Cu K_α radiation (α = 0.154056 nm) at 40 kV and 40 mA. Figure 2a shows the XRD patterns of laser-treated samples (P_0.4 black, P_0.5 red). The detected reflections correspond to Ti, with characteristic peaks at 35, 38, 40 and 52.5 °2Theta). No additional phases were detected. Peak identification was performed using the ICDD PDF database[20] and crystallographic open database COD[21].

Element	P_0.4 [% at]	P_0.5 [% at]
Ti	69.32 ± 7.98	74.29 ± 8.37
O	30.68 ± 9.32	25.71 ± 8.12

Table 2. Surface chemical composition analysed by EDS.

a result, a rough surface with a characteristic and unique morphology is formed (Fig. 1b and e). In Fig. 1c and f this surfaces are shown at a scale of 1 µm. From this image it can be concluded that the surface is represented by spherical-like formations covered with smaller structures of nanometric scale, which are oxidation products. It was confirmed by EDS measurements, given in Table 2. The chemical composition indicate that contents of oxide layer is negligible.

The laser-treated samples (P_0.4, P_0.5; Fig. 2b - e) were analysed by Raman spectroscopy to assess the composition of the surface layer, with particular focus on titanium oxides. The spectra confirmed the presence of TiO_2 on both P_0.4 and P_0.5. Several characteristic Raman bands of TiO_2 were identified, corresponding to the anatase and rutile crystal phases. For anatase, vibrational modes were observed at 146 cm^{-1} (E_g), 394 cm^{-1} (B_{1g}). 512 cm^{-1} (A_{1g}). and 635 cm^{-1} (E_g). Bands corresponding to rutile were also detected, with active vibrational modes at 141 cm^{-1} (B_{1g}), 244 cm^{-1} (E_g). 442 cm^{-1} (E_g) and 610 cm^{-1} (A_{1g})[22]. The precise spectral positions and their phase assignments are summarized in Table 3.

The surface chemical composition and spatial distribution on laser-treated titanium samples were characterized by ToF-SIMS, revealing significant modifications compared to untreated controls (Fig. 4). The analyses demonstrated pronounced oxygen-enriched lines that correspond to the laser interference pattern with a spatial period of approximately 50 µm. This pattern reflects the localized oxidation driven by the laser intensity distribution, where the Gaussian profile of the beam influences the width and intensity of the oxygen-rich regions. Depth profiles further confirmed a substantially thicker titanium oxide layer induced by laser processing relative to native oxide layers on untreated samples. The titanium oxo-clusters detected by ToF-SIMS decreased progressively with depth, indicating surface localization of the oxide layer. Various titanium oxo clusters (TiO_3^-, TiO_2^-, TiO^-) have been observed on the sample surfaces (Fig. 3a, b). Their intensity decreases as deeper layers of the sample are reached. This chemical modification may enhance the surface bioactivity by modulating protein adsorption and cellular interactions. The substantial oxide growth and chemical changes induced by ultrashort pulsed laser treatment strongly correlate with improved wettability and hydrophilicity of the titanium surface, factors known to support protein layer preservation and osteoblast adhesion. The combination of micro- and nano-scale topographical features and reactive surface chemistry established by laser interference patterning thus yields a favourable microenvironment for enhanced cell proliferation and osseointegration, as supported by biological assays[23].

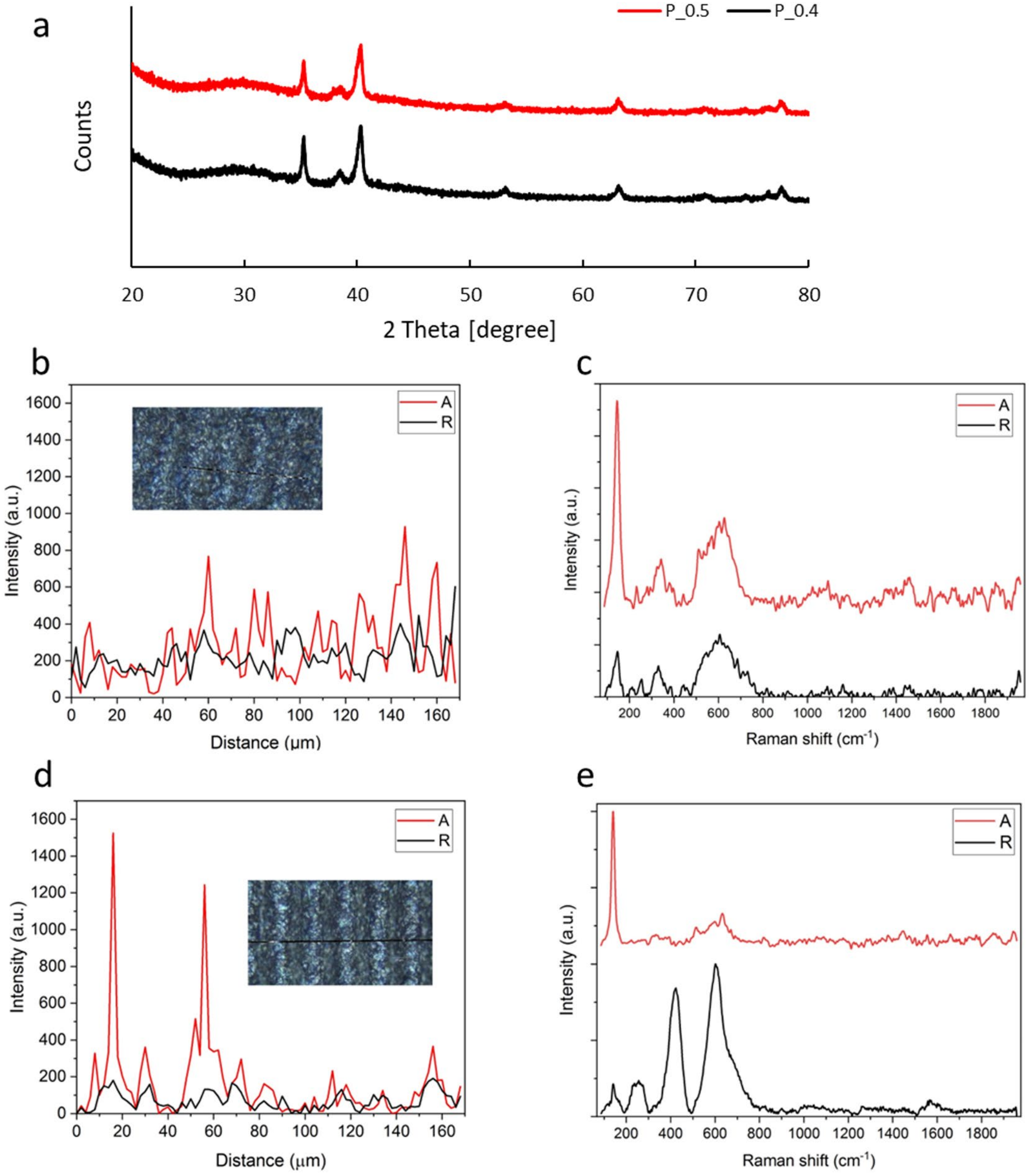

Fig. 2. XRD pattern of samples surfaces P_0.4 (black), P_0.5 (red) (**a**); Raman spectra anatase (red), rutile (black) on P_0.4 (b, c), P_0.5 (d, e) surfaces.

Band position (cm^{-1})	Band identification	Crystal structure
141	B_{1g}	Rutile
146	E_g	Anatase
244	E_g	Rutile
394	B_{1g}	Anatase
442	E_g	Rutile
512	A_{1g}	Anatase
610	A_{1g}	Rutile
635	E_g	Anatase

Table 3. Frequencies and assignments of Raman bands for anatase and rutile phases.

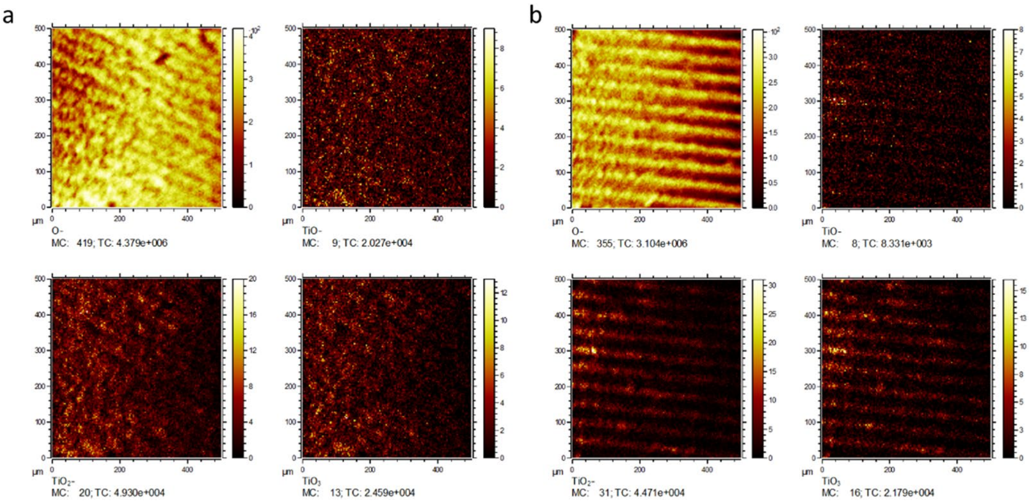

Fig. 3. ToF-SIMS images showing the depth-integrated top views of the secondary ion distributions of O- and titanium oxides clusters (TiO^-, TiO_2^-, TiO_3^-) in P_0.4 (a) and P_0.5 (b) samples.

XRD measurements results indicating that the formed oxide layer was either amorphous, nanocrystalline below the detection limit, or too thin for diffraction. Observed Raman active vibrational modes for anatase and rutile confirming surface oxidation even though these phases were not detected by XRD. The preservation of the bulk titanium crystal structure after laser modification is critical for maintaining the mechanical integrity of the implant while providing beneficial surface chemical modifications. The slight surface oxidation induced by the nanosecond laser is sufficient to create mixed titanium oxide clusters (TiO_3^-, TiO_2^-, TiO^-) as demonstrated by ToF-SIMS, which contributes to surface bioactivity without compromising the substrate's crystallinity. The obtained XRD results indicate that nanosecond laser treatment effectively modifies the surface chemistry by generating oxides while preserving the crystalline titanium core. This balance between surface oxidation and core structural stability provides a promising platform for developing multifunctional implant surfaces with enhanced biocompatibility and controlled photocatalytic activity.

Surface properties of biomaterials, including their chemistry, topography and wettability, are widely regarded as key factors influencing cellular reaction at biomaterial surfaces[24]. Surface roughness is a factor significantly influencing the capacity of materials to support cell adhesion[25–27]. Shalabi et al.[28] found a positive correlation between bone-to-implant contact and implant surface roughness. Nano-scale roughness closely resembles natural tissue morphology and is regarded as a key factor promoting cell adhesion, growth, and maturation. For instance, studies on human venous endothelial cells have shown that increasing nanometric surface roughness enhances both adhesion and proliferation[29]. Importantly, it was also shown that surface roughness on micron and submicron scales exert positive effect on cell adhesion[30,31]. For instance, Deng et al.[32] revealed that moderate surface roughness – in the range of 1.96–2.95 µm – had the ability to increase human osteosarcoma cells attachment and proliferation. Roughness analysis performed using the LEXT™ OLS5100 3D Laser Scanning Microscope showed that the sample P_0.4 (Fig. 4) had nearly half the surface roughness (1.57 µm) compared to the P_0.5 (2.72 µm). In the conducted test, tissue culture–treated coverslips were used as control samples due to their favourable conditions for cell attachment and growth. All tested samples possessed the micro-scale roughness, which is known to support cell adhesion. The tested materials exhibited a hydrophobic surface, with an average contact angle of approximately 140°, which was nearly twice as high as that of the control (Fig. 4).

Photocatalytic activity of surfaces

The photocatalytic activity of the surfaces was evaluated through the degradation of MB solution under weakly acidic conditions (pH 6) in air. Figure 5a shows the MB decay for photocatalytic and control experiments. The dye degradation observed on P_0.4 and P_0.5 surfaces was only 1.5–2%, falling within the measurement error margin.

Hence, the photocatalytic activity of the laser-structured surfaces are low (k_{app} value was 0.3×10^{-3}, 0.6×10^{-3} and 1.5×10^{-3} min^{-1} for K, P_0.4 and P_0.5, respectively) (Fig. 5b).

Barylak et al. in their recent article[22] presents the photocatalytic activity of the Ti surface treated by a femtosecond laser. Different morphology of surfaces were obtained applying different laser processing regimes (energy per pulse 8 and 4 µJ; pulse frequency 500 and 1000 kHz; step 5 and 10 µm for spikes and groves structures, respectively). Both samples (spikes and groves) possess a high amount of oxygen (> 40% at). The photocatalytic activity of the samples was higher than in the present work and the determined rate constants were 16.2×10^{-3} and 26.7×10^{-3} min^{-1} for spikes and groves, respectively. Observed differences for apparent rate constant values are caused by a lower amount of oxides on the surfaces obtained in present work. Due to the weak photocatalytic activity of the tested surfaces, P_0.4 and P_0.5, it can be assumed that these surfaces, under conditions of cell colonisation, will not generate reactive forms that could adversely affect cell development.

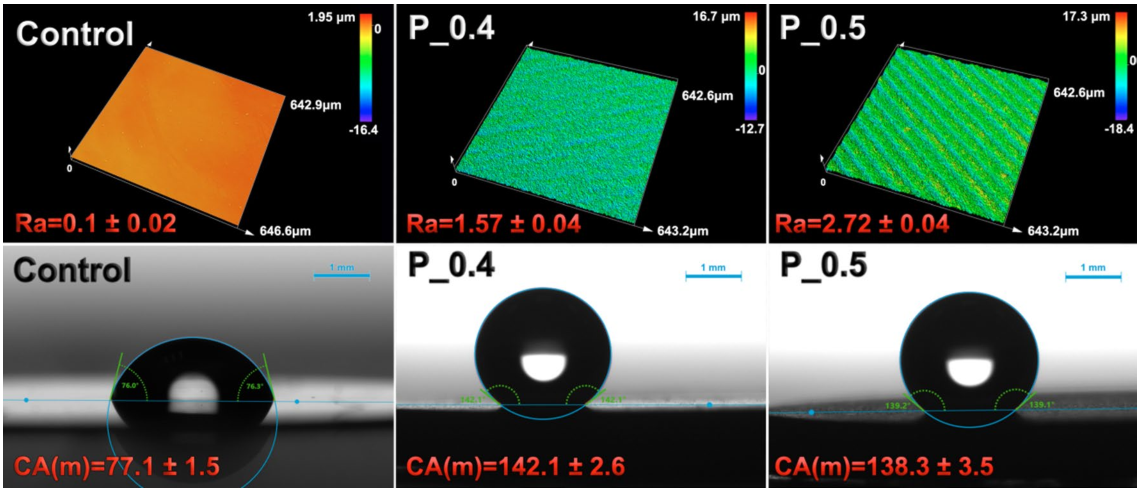

Fig. 4. Top row – topography of the control (tissue culture-treated coverslip), P_0.4 and P_0.5 sample surfaces and their roughness profile (R_a in µm) measured using confocal laser scanning optical profilometer; bottom row – goniometer images showing the contact angle of an ultrapure water droplet on the top surfaces of the control, P_0.4 and P_0.5 samples.

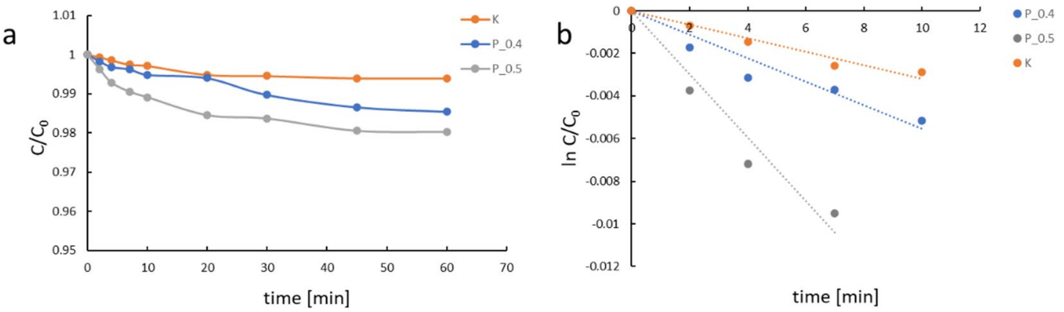

Fig. 5. (a) Plot of the relative concentrations (C_t/C_0) vs. time of MB solution on surfaces P_0.4 (grey), P_0.5 (blue) and MB photolysis as control (orange); (b) the dependence of $\ln(C/C_0)$ on time for samples P_0.4 (grey), P_0.5 (blue).

Evaluation of biomaterial biocompatibility

Numerous studies, including clinical ones, indicated very good biocompatibility and tissue compatibility of materials made of titanium and most of its alloys[33]. Cytotoxicity of the biomaterials was determined in direct contact using the colorimetric LDH release test. The in vitro experiment showed that the biomaterials were non-toxic to mouse preosteoblasts (MC3T3-E1 cells line). The amount of released LDH was comparable to control cells indicating the cells cultured on the tested samples were viable and maintained cell membrane integrity (P_0.4 = 104% and P_0.5 = 108% compared to the control cells) (Fig. 6a).

The lack of cytotoxicity to mouse preosteoblasts was also confirmed by fluorescent Live/Dead staining. It was observed that after 48 h of culture, the surface of the tested materials was covered with viable cells (emitting green fluorescence), flattened at a density similar to the control (Fig. 6b).

The ability of biomaterials to stimulate cell proliferation on its surface was assessed using the WST-8 test. After 96 h of incubation, a statistically significant lower number of cells was demonstrated on the surface of the P_0.4 material (1.7×10^3 cells per material) compared to the control (2.2×10^3 cells per material) (Fig. 7a). However, an increase in the number of cells over time was observed on the surface of both P_0.4 and P_0.5 samples, indicating that the materials supported cell adhesion and growth on their surfaces (Fig. 7b). Fluorescent staining of the cytoskeleton at three time intervals revealed a comparable number of cells on the surfaces of the control (tissue culture-treated coverslip) and tested materials during the first two days of the test. After 96 h of incubation, the number of cells on the surface of the control was higher than on the P_0.4 and P_0.5 materials. The studies showed improved adhesion and increased cell spreading with enhanced surface hydrophilicity[34]. Another parameter, the increase of which is correlated with the improvement of cell adhesion, is the roughness of the surface[35]. The lower density of cells on the surface of the tested samples compared to the control could result from the hydrophobic nature of the materials. However, samples P_0.4 and P_0.5 still allowed for good adhesion and proliferation of mouse preosteoblasts and were non-toxic, which indicated their good biocompatibility. No significant difference in cellular response was noted between the tested samples.

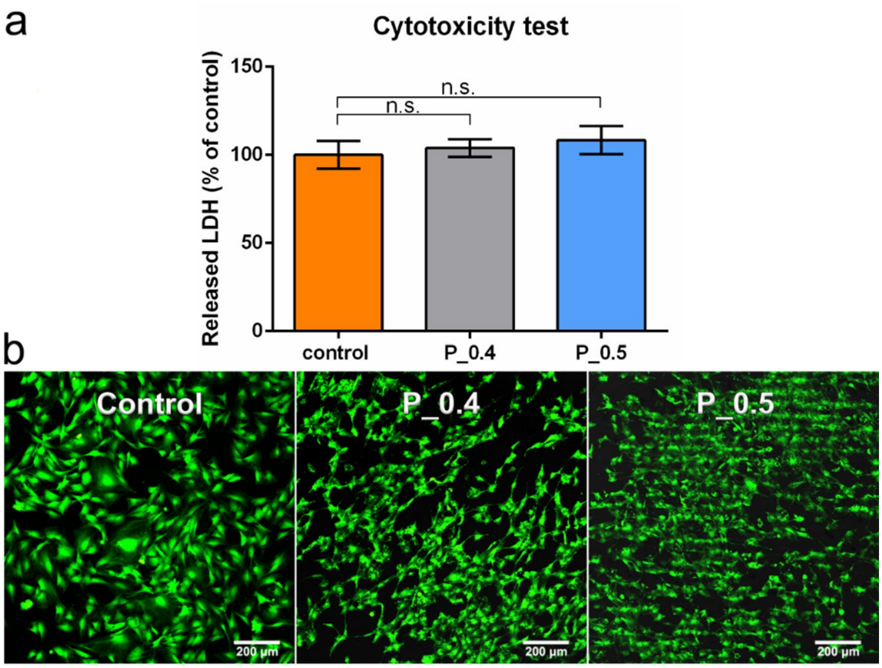

Fig. 6. LDH release cytotoxicity test performed in direct contact after 48 h of culture (control – cell cultured on tissue culture-treated coverslip) (a), CLMS images of cells on the material after 48 h of incubation stained with the Live/Dead kit (green fluorescence - viable cells, red - dead cells) (b); n.s. - demonstrated no statistical significance between indicated groups, $p > 0.05$, $n = 3$.

Cell adhesion to a biomaterial surface is a multi-stage process that determines biological activities and even cell survival. Important biomaterial properties that influence cell adhesion beyond roughness and wettability, include surface charge, stiffness, chemical functionality and material degradation[36,37]. Improving one parameter can significantly alter cell behavior despite the unfavorable properties of another parameter. For instance, S. M. Kang et al.[38] increased the surface energy of a highly hydrophobic material using polydopamine modification. It was observed that cells selectively adhered only to fragments of the superhydrophobic surface coated with polydopamine. It is well known that a surface with a rough texture supports cell adhesion compared to smooth surfaces[29]. In this study, controlled micro- and nano-structuring of the biomaterial using a laser was used to enhance its roughness. The demonstrated good cell adhesion can likely be attributed to the increased roughness achieved through surface modification. Improvement of surface topography by increasing the roughness was able to compensate the unfavorable effect of hydrophobicity, which is known to hinder cell adhesion[36]. It is also worth considering that it has recently been demonstrated that protein adsorption to a hydrophobic surface is possible via direct interactions with hydrophobic fragments on the protein surface as well as via internal hydrophobic residues exposed by protein denaturation[36]. Further studies should be conducted to extend the characterization and confirm the biomedical potential of the samples.

Crucially, our WST-8 assays and fluorescent cytoskeletal staining show that preosteoblasts adhere, spread, and proliferate on these moderately oxidized, hydrophobic surfaces at rates comparable to tissue-culture controls. This finding revises established hypotheses regarding the prerequisites for optimal cellular response, demonstrating that maximal surface oxidation and inherent superhydrophilicity are not universal necessities for achieving the best biological outcomes. By decoupling biocompatibility from extreme surface oxidation, our nanosecond laser strategy offers a cost-effective, scalable alternative to femtosecond approaches, broadening the design space for implant surface engineering.

Despite extensive research studies, a comprehensive understanding of the mechanisms that regulate cell attachment to biomedical surfaces remains incomplete[39,40]. Nevertheless, based on the data presented in Table 4, a thorough analysis reveals complex yet discernible correlations between surface topography (S_a/R_a), surface chemistry (oxygen content), wettability (WCA), and subsequent biological responses (cell adhesion/proliferation). The data strongly suggest that there is no singular optimal roughness value; rather, the biological outcome is critically dependent on how roughness interacts with surface chemistry and wettability. The "Best" cell adhesion results are observed at specific, low S_a values when coupled with super-hydrophilicity (WCA ≈ 0°) (samples A1, B6)[16]. This indicates that for extremely hydrophilic surfaces, a low micro/nano roughness profile is ideal for promoting initial adhesion. Excessive roughness appears detrimental to cellular behaviour, even when wettability is otherwise favorable. High roughness (S_a exceeding 10 µm)[17] acts as a physical barrier, disrupting necessary cell-surface contact and overriding the positive effect of wettability (see sample R_d). When the surface is hydrophobic (WCA > 100°)[23], increased roughness often hinders performance, as seen in the case of samples 3.1 and 3.2.

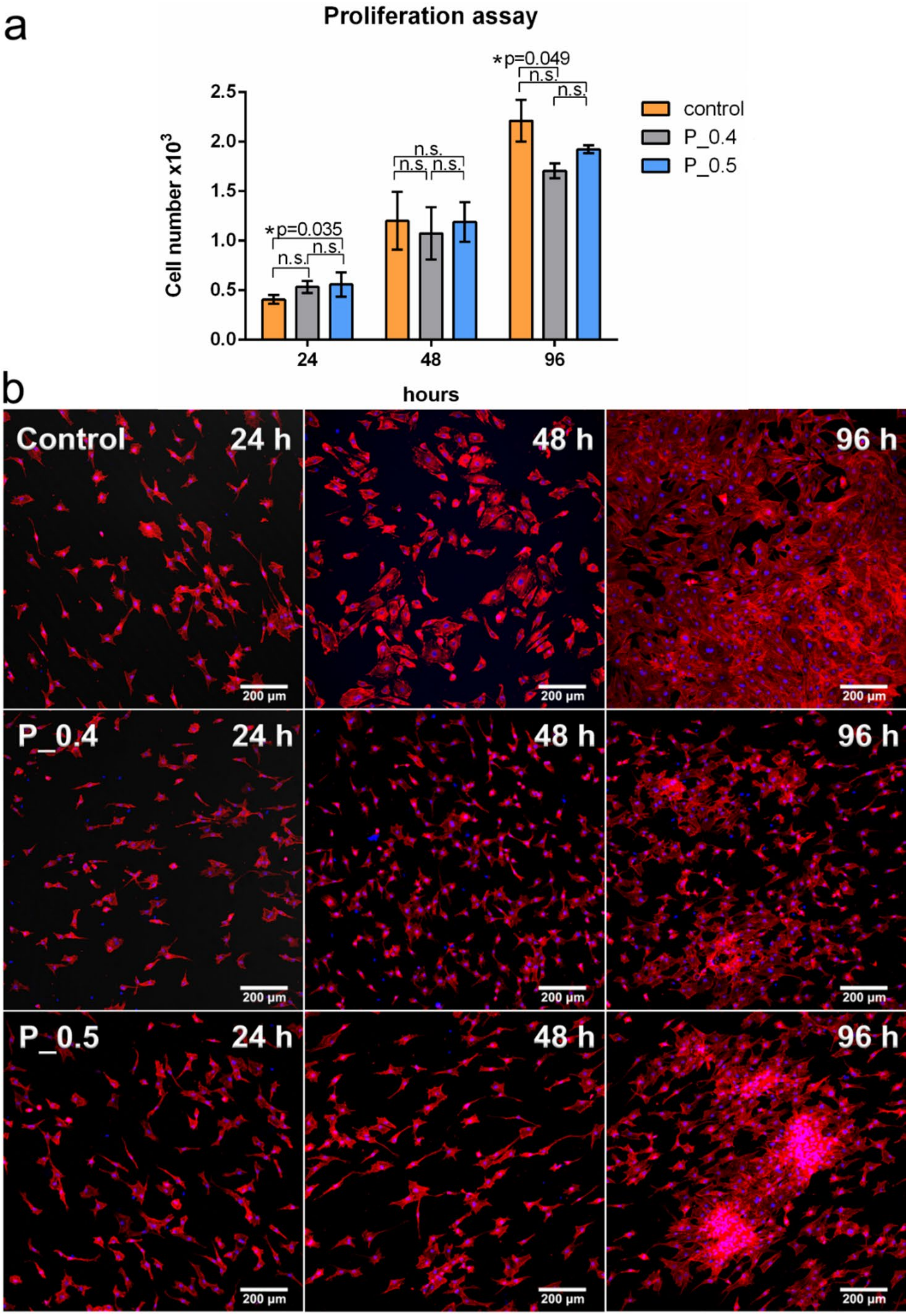

Fig. 7. Proliferation assessed by the WST-8 test in direct contact (control – cell cultured on tissue culture-treated coverslip) (a); CLSM images of cells cultured for 24 h, 48 h, 96 h on the surface of material after fluorescent cytoskeleton staining (nuclei – blue fluorescence, actin filaments – red fluorescence) (b) (* demonstrated statistically significant results between indicated groups, $p \leq 0.05$, $n = 3$, one-way ANOVA followed by Tukey's test, n.s. - demonstrated no statistical significance between indicated groups, $p > 0.05$, $n = 3$).

This indicates that in highly hydrophobic environments, a smooth surface is preferred, likely to avoid excessive air trapping (Cassie state), which could interfere with protein adsorption and cellular anchoring. The data collected in Table 4 demonstrates successful cell adhesion outcomes across both highly hydrophilic and highly hydrophobic regimes, indicating that extremity in wettability is often preferred over moderate values.

Super-hydrophilicity (WCA ≈ 0 to 5°, samples A1, B1, B6)[16] yields "good" or "best" results of cell adhesion/proliferation. Super-hydrophilic surfaces favour the rapid adsorption of water and small, highly ordered protein layers, which typically promote cell attachment. Contrary to simple assumptions, highly hydrophobic surfaces (WCA > 130°, samples: Fs-random, Fs-organized, P_0.4, P_0.5)[14] also support good cell adhesion. This efficacy

Literature	Laser	Pulse duration	Material	Samples name	Roughness S_a/R_a	Oxygen content (% at)	WCA* (°)	Cell adhesion/ Cell proliferation#
[14]	GF Laser P 400 U fs 1030 nm	300 fs	Ti-6Al-4 V	Fs-random	1.43	No data	151.2	Good
				Fs-organized	1.52	No data	159.7	Good
[16]	Nd: YVO$_4$ 355 nm	50 ns	Ti-6Al-4 V	A1	0.3	8.40	4.8	Best
				A2.5	1.28	11.63	4.4	Good
				A4	3.64	17.24	2.5	Good
				A6	5.26	7.09	2.5	Good
				B1	8.08	10.42	0	Good
				B2.5	7.27	9.35	0	Good
				B4	4.48	8.06	0	Good
				B6	2.15	6.41	0	Best
[17]	Nd: YVO$_4$ 355 nm	50 ns	Ti-6Al-4 V	G_s	5.99	46.82	0	Good
				G_l	5.57	48.34	48	Good
				B_et	5.25	46.13	21	Good
				R_d	10.96	45.65	0	Poor
[23]	Nd: YVO$_4$ 1064 nm	10 ps	Ti-6Al-4 V	3.1	0.21	0.43	> 100	Good
				3.2	0.84	1.00	> 100	Poor
				10.1	0.21	0.4	50 < CA < 100	Poor
				10.2	0.47	0.63	50 < CA < 100	Moderate
				17.1	0.19	0.25	< 50	Moderate
				17.2	0.58	0.89	< 50	Good
[41]	Nd: YAG 532 nm	10 ns	cpTi (grade 2 and grade 4)	Ti2L	0.31	No data	66	Poor
				nTi2L	0.28	No data	66	Poor
				Ti4L	0.26	No data	65	Moderate
				nTi4L	0.26	No data	68	poor
	Ti: Sapphire 800 nm	100 fs		Ti2F	0.34	No data	52	Poor
				nTi2F	0.25	No data	52	Poor
				Ti4F	0.25	No data	51	Moderate
				nTi4F	0.26	No data	51	Moderate
This work	Nd: YAG fiber laser 1064 nm	120 ns	cpTi (grade 4)	P_0.4	1.57	30.68	142	Good
				P_0.5	2.72	25.71	138	Good

Table 4. Studies on surface modification by femtosecond and nanosecond lasers. * - WCA – wettability contact angle. # - this scale was arbitrary established by authors.

is often attributed to the favourable conformation of specific cell-adhesion proteins (e.g., fibronectin) adsorbed onto hydrophobic interfaces. Moderate wettability (100°> WCA > 50°) generally correlates with poor or moderate adhesion/proliferation. This confirms that surfaces with intermediate wettability often lack the distinct physical/chemical driving force required for optimal cellular response or controlled protein layer formation.

Oxygen content, typically reflecting the thickness and composition of the thermally induced oxide surface layer, exhibits a complex relationship with cell adhesion. High oxygen levels are often associated with superhydrophilicity (G_s, R_d)[17]. Adhesion is generally "good" (e.g., G_s, B_et), unless roughness is excessive (R_d). This means that a thick, highly oxygenated surface layer is favourable for adhesion, primarily due to the resulting surface energy/wettability. The highly successful hydrophilic samples A1 ("best") and B6 ("best")[16] exhibit lower oxygen content (A1: 8.40 at%; B6: 6.41 at%) than the G_s, B_et, R_d group. This suggests that achieving superhydrophilicity and "best" results does not necessarily require the highest bulk oxidation state; rather, it requires a specific, favourable local architecture. In contrast, the successful hydrophobic nanosecond samples (P_0.4, P_0.5) maintain moderate oxygen content (25.71 and 30.68 at%).

Optimal cell adhesion may be achieved in two distinct, extreme regimes: (i) hydrophilic-smooth - characterized by super-hydrophilicity (WCA ≈ 0 to 5°) combined with low roughness ($S_a \approx 0.3$ to 2.2 μm) and moderate oxygen content (< 10 at%); (ii) hydrophobic-rough - characterized by high hydrophobicity (WCA > 140°) combined with moderate roughness (< 3 μm). Excessive roughness exceeding the apparent critical threshold ($S_a > 10$ μm, as seen in R_d) is detrimental regardless of the very favourable wettability.

Hydrophobic, moderately oxidized titanium surfaces can promote preosteoblast adhesion primarily through enhanced protein adsorption mediated by surface roughness and topographical features[41]. Traditionally, superhydrophilicity and high surface oxidation are believed to promote cell adhesion, but recent studies have shown that nano- and micro-scale roughness significantly influences the conformation and retention of extracellular matrix proteins, such as fibronectin and vitronectin, which mediate integrin binding and cell anchoring[42,43]. Hydrophobic surfaces with hierarchical roughness can promote selective adsorption of adhesion-promoting proteins in conformations that favour cell receptor recognition, effectively compensating for reduced wettability[44]. Additionally, moderate oxidation provides a stable titanium oxide layer that maintains corrosion resistance and bioactivity without the excessive reactive oxygen species generation associated with highly oxidized, superhydrophilic surfaces, which can be detrimental to cell viability. Thus, the interplay between surface roughness-induced protein adsorption and moderate, stable oxide chemistry creates a favourable microenvironment for preosteoblast attachment, spreading, and proliferation despite the apparent hydrophobic character of the surface. This aligns with emerging evidence highlighting the primacy of topographical and biochemical cues over absolute wettability in regulating early osteogenic responses. Thus, the central innovation in surface engineering lies not in maximising a single parameter, but in achieving an optimal hierarchical interplay between these factors.

Conclusion

This study introduces a methodologically significant and cost-effective method for engineering titanium implant surfaces utilizing a streamlined, single-step nanosecond laser treatment. Rigorous analytical confirmation, achieved through techniques such as SEM, EDS, XRD, Raman spectroscopy, and ToF-SIMS analysis, revealed that the nanosecond laser structuring effectively generates diverse surface topographies (including micro-grooves, ripples, and spikes) alongside mixed anatase-rutile titanium oxide phases.

The functional assessment of the tested hydrophobic samples (P_0.4 and P_0.5) confirmed they were non-toxic to cells. They provided a surface environment that effectively supported preosteoblast adhesion, spreading, and proliferation. This result is particularly significant as it demonstrates functional efficacy equivalent to or comparable with the more complex and costly femtosecond (fs) laser methods tested in the same hydrophobic regime (e.g., Fs-random/Fs-organized samples).

The nanosecond laser technology exhibits a sophisticated capability for dual functionalization: achieving superior performance in the super-hydrophilic regime *via* controlled oxidation and low roughness, while simultaneously achieving equivalent functional performance to fs lasers in the hydrophobic domain. Future efforts should focus on fine-tuning surface features and validating their long-term clinical performance in vivo.

Data availability

All data generated or analysed during this study are included in this published article (and its Supplementary Information files).

Received: 12 October 2025; Accepted: 29 January 2026

References

1. Jemat, A., Ghazali, M. J., Razali, M. & Otsuka, Y. Surface modifications and their effects on titanium dental implants. *Biomed. Res. Int.* **2025**, 791725. https://doi.org/10.1155/2015/791725 (2015).
2. Mouhyi, J., Dohan Ehrenfest, D. M. & Albrektsson, T. The Peri-Implantitis: implant surfaces, microstructure, and physicochemical aspects. *Clin. Implant Dent. Relat. Res.* **14** (2), 170–183. https://doi.org/10.1111/j.1708-8208.2009.00244.x (2012).
3. Rozé, J. et al. Correlating implant stability to bone structure. *Clin. Oral Implants Res.* **20** (10), 1140–1145. https://doi.org/10.1111/j.1600-0501.2009.01745.x (2009).
4. Palmquist, A., Omar, O. M., Esposito, M. & Lausmaa, Thomsen, J. Titanium oral implants: surface characteristics, interface biology and clinical outcome. *J. R Soc. Interface.* **7** (5), 515–527. https://doi.org/10.1098/rsif.2010.0118.focus (2010).
5. Zambuzzi, W. F. et al. Nanometer scale titanium surface texturing are detected by signaling pathways involving transient FAK and Src activations. *PLoS One.* **9**, e95662. https://doi.org/10.1371/journal.pone.0095662 (2014).
6. Park, J. W., Han, S. H. & Hanawa, T. Effects of surface nanotopography and calcium chemistry of titanium bone implants on early blood platelet and macrophage cell function. *Biomed. Res. Int.* **1362958**, 10. https://doi.org/10.1155/2018/1362958 (2018).
7. Coelho, P. G., Jimbo, R., Tovar, N. & Bonfante, E. A. Osseointegration hierarchical designing encompassing the macrometer, micrometer, and nanometer length scales. *Dent. Mater.* **31**, 37–52. https://doi.org/10.1016/j.dental.2014.10.007 (2015).
8. Xu, R. et al. Micro-/nano-topography of selective laser melting titanium enhances adhesion and proliferation and regulates adhesion-related gene expressions of human gingival fibroblasts and human gingival epithelial cells. *Int. J. Nanomed.* **13**, 5045–5057. https://doi.org/10.2147/IJN.S166661 (2018).
9. Yoo, D. et al. Increased osseointegration effect of bone morphogenetic protein 2 on dental implants: an in vivo study. *J Biomed. Mater. Res. A.* **102**, 1921–1927. https://doi.org/10.1002/jbm.a.34862 (2014).
10. Lackington, W. A. et al. Femtosecond Laser-Texturing the surface of Ti-Based implants to improve their osseoitegration capacity. *Adv. Mat. Interfac.* **9** (31), 2201164. https://doi.org/10.1002/admi.202201164 (2022).
11. Ionescu, A. C. et al. Laser microtextured titanium implant surfaces reduce in vitro and in situ oral biofilm formation. *PLoS One.* **13** (9), e0202262. https://doi.org/10.1371/journal.pone.0202262 (2018).
12. Saran, R., Ginjupalli, K., George, S. D. & Chidangil, S. LASER as a tool for surface modification of dental biomaterials: a review. *Heliyon* **9** (6), e17457. https://doi.org/10.1016/j.heliyon.2023.e17457 (2023).
13. Tsai, M. H. et al. Surface modification induced phase transformation and structure variation on the rapidly solidified recast layer of titanium. *Mater. Charact.* **106**, 463–469. https://doi.org/10.1016/j.matchar.2015.06.004 (2015).
14. Lackington, W. A. et al. Femtosecond Laser-Texturing the surface of Ti-Based implants to improve their osseointegration capacity. *Adv. Mater. Interf.* **9** (31), 2201164. https://doi.org/10.1002/admi.202201164 (2022).
15. Liu, Y. et al. Characterization and evaluation of a femtosecond laser-induced osseointegration and an anti-inflammatory structure generated on a titanium alloy. *Regen Biomater.* **8** (2), rbab006. https://doi.org/10.1093/rb/rbab006 (2021).
16. Wang, Y., Yu, Z., Li, K. & Hu, J. Study on the effect of surface characteristics of short-pulse laser patterned titanium alloy on cell proliferation and osteogenic differentiation. *Mater. Sci. Eng. C* **128**, 112349. https://doi.org/10.1016/j.msec.2021.112349 (2021).
17. Wang, Y., Zhang, M., Li, K. & Hu, J. Study on the surface properties and biocompatibility of nanosecond laser patterned titanium alloy. *Opt. Laser Technol.* **139**, 106987. https://doi.org/10.1016/j.optlastec.2021.106987 (2021).
18. Sypniewska, J. & Szkodo, M. Influence of laser modification on the surface character of biomaterials: titanium and its alloys. – *Rev. Coat.* **12** (10), 1371. https://doi.org/10.3390/coatings12101371 (2022).
19. https://www.graphpad.com/ (2023, assessed 15 May 2023).
20. Kabekkodu, S. & PDF-4+ (Database). *International Centre for Diffraction Data* (Newtown Square, 2015).
21. Crystallography Open Database (2021, accessed 5 Sep 2021). http://www.crystallography.net/cod/.

22. Barylyak, A. et al. Photocatalytic and antibacterial activity properties of Ti surface treated by femtosecond laser – a prospective solution to peri-implant disease. *Sci. Rep.* **14**, 20926. https://doi.org/10.1038/s41598-024-70103-4 (2024).
23. Zwahr, C. et al. Ultrashort pulsed laser surface patterning of titanium to improve osseointegration of dental implants. *Adv. Eng. Mater.* **21**, 1900639. https://doi.org/10.1002/adem.201900639 (2019).
24. Ranella, A., Barberoglou, M., Bakogianni, S., Fotakis, C. & Stratakis, E. Tuning cell adhesion by controlling the roughness and wettability of 3D micro/nano silicon structures. *Acta Biomater.* **6**, 2711–2720. https://doi.org/10.1016/j.actbio.2010.01.016 (2010).
25. Singh, A. V. et al. Bottom-up engineering of the surface roughness of nanostructured cubic zirconia to control cell adhesion. *Nanotechnology* **23** (47), 475101. https://doi.org/10.1088/0957-4484/23/47/475101 (2012).
26. Amani, H. et al. Controlling cell behavior through the design of biomaterial surfaces: a focus on surface modification techniques. *Adv. Mater. Interfaces*. **6**, 1900572. https://doi.org/10.1002/admi.201900572 (2019).
27. Yang, W., Yu, H., Li, G., Wang, Y. & Liu, L. Facile modulation of cell adhesion to a poly(ethylene glycol) diacrylate film with incorporation of polystyrene nano-spheres. *Biomed. Microdevices*. **18** (6), 107. https://doi.org/10.1007/s10544-016-0133-4 (2016).
28. Shalabi, M. M., Gortemaker, A., Van't Hof, M. A. & Jansen, J. A. Creugers, N.H.J. Implant surface roughness and bone healing: a systematic review. *J. Dent. Res.* **85** (6), 496–500. https://doi.org/10.1177/154405910608500603 (2006).
29. Chung, T. W., Liu, D. Z., Wang, S. Y. & Wang, S. S. Enhancement of the growth of human endothelial cells by surface roughness at nanometer scale. *Biomaterials* **24** (25), 4655–4661. https://doi.org/10.1016/s0142-9612(03)00361-2 (2003).
30. Cai, S. et al. Recent advance in surface modification for regulating cell adhesion and behaviors. *Nanotechnol Rev.* **9** (1), 971–989. https://doi.org/10.1515/ntrev-2020-0076 (2020).
31. Sachot, N., Engel, E. & Castano, O. Hybrid organic-inorganic scaffolding biomaterials for regenerative therapies. *Curr. Org. Chem.* **18**, 2299–2314. https://doi.org/10.2174/1385272819666140806200355 (2014).
32. Deng, Y. et al. Effect of surface roughness on osteogenesis in vitro and osseointegration in vivo of carbon fiber-reinforced polyetheretherketone–nanohydroxyapatite composite. *Int. J. Nanomed.* **10** (1), 1425–1447. https://doi.org/10.2147/IJN.S75557 (2015).
33. Hanawa, T. Biocompatibility of titanium from the viewpoint of its surface. *Sci. Technol. Adv. Mater.* **23** (1), 457–472. https://doi.org/10.1080/14686996.2022.2106156 (2022).
34. Ponsonnet, L. et al. Relationship between surface properties (roughness, wettability) of titanium and titanium alloys and cell behaviour. *Mater Sci. Eng. C.* **23** (4), 551–560. https://doi.org/10.1016/S0928-4931(03)00033-X (2003).
35. Stepanovska, J., Matejka, R., Rosina, J., Bacakova, L. & Kolarova, H. Treatments for enhancing the biocompatibility of titanium implants. *Biomed. Pap Med. Fac. Univ. Palacky Olomouc Czech Repub.* **164** (1), 23–33. https://doi.org/10.5507/bp.2019.062 (2020).
36. Ferrari, M., Cirisano, F. & Moran, C. Mammalian cell behavior on hydrophobic substrates: influence of surface properties. *Colloids Interfaces*. **3** (2), 48. https://doi.org/10.3390/colloids3020048 (2019).
37. Oliveira, S. M., Alves, N. M. & Mano, J. F. Cell interactions with superhydrophilic and superhydrophobic surfaces. *J. Adhes. Sci. Technol.* **28** (8–9), 843–863. https://doi.org/10.1080/01694243.2012.697776 (2012).
38. Kang, S. M. & Choi, I. S. Control of cell adhesion on a superhydrophobic surface by polydopamine coating. *Bull. Korean Chem. Soc.* **34** (8), 2525–2527. https://doi.org/10.5012/bkcs.2013.34.8.2525 (2013).
39. Lee, J., Cuddihy, M. J. & Kotov, N. A. Three-dimensional cell culture matrices: state of the Art. *Tissue Eng. Part. B Rev.* **14** (1), 61–68. https://doi.org/10.1089/teb.2007.01 (2008).
40. Seidlits, S. K., Lee, J. Y. & Schmidt, C. E. Nanostructured scaffolds for neural applications. *Nanomedicine* **3** (2), 183–199. https://doi.org/10.2217/17435889.3.2.183 (2008).
41. Nekleionova, A. et al. Comparative study of cell interaction and bacterial adhesion on titanium of different composition, structure and surfaces with various laser treatment. *Mater. Res. Express.* **11**, 055403. https://doi.org/10.1088/2053-1591/ad45be (2024).
42. Luo, J. et al. The influence of nanotopography on cell behaviour through interactions with the extracellular matrix-A review. *Bioactive Mater.* **15**, 145–159. https://doi.org/10.1016/j.bioactmat.2021.11.024 (2022).
43. Barberi, J. & Spriano, S. Titanium and protein adsorption: an overview of mechanisms and effects of surface features. *Materials* **14** (7), 1590. https://doi.org/10.3390/ma14071590 (2021).
44. Zhou, K. et al. Effect of surface energy on protein adsorptionbehaviours of treated CoCrMo alloy surfaces. *Appl. Surf. Sci.* **520**, 146354. https://doi.org/10.1016/j.apsusc.2020.146354 (2020).

Acknowledgements

Wettability test, surface roughness analysis, and biological characterization were funded by the Ministry of Science and Higher Education in Poland within the statutory activity of the Medical University of Lublin (DS 630 project).

Author contributions

A. B. contributed to investigation, methodology, writing original draft; S.M. contributed to Ti surfaces structuration; A.L. contributed to Ti surfaces structuration; P. K. contributed to EDS and SEM measurements; R. W.-N. contributed to Raman measurements, data interpretation; M. T.-S. contributed to ToF SIMS measurements; M.T. contributed to investigation of toxicity and biocompatibility, writing original draft; V.V. contributed to roughness measurements, wettability test, writing original draft; B. C. contributed to XRD measurements; A. P. contributed to methodology, critical revision of the final draft of the manuscript, supervision; (A) D. contributed to SEM measurements and data interpretation; Y. (B) contributed to the conception of laser treatment, writing the original draft; J. K. contributed to conceptualisation, methodology, investigation, writing original draft, writing – review & editing, supervision.

Funding

Wettability test, surface roughness analysis, and biological characterization were funded by the Ministry of Science and Higher Education in Poland within the statutory activity of the Medical University of Lublin (DS 630 project).

Competing interests

Joanna Kisała declare existing conflict of interest due to being a member of the Scientific Reports editorial board.

Additional information

Supplementary Information The online version contains supplementary material available at https://doi.org/1

0.1038/s41598-026-38369-y.

Correspondence and requests for materials should be addressed to J.K.

Reprints and permissions information is available at www.nature.com/reprints.

Publisher's note Springer Nature remains neutral with regard to jurisdictional claims in published maps and institutional affiliations.

Open Access This article is licensed under a Creative Commons Attribution-NonCommercial-NoDerivatives 4.0 International License, which permits any non-commercial use, sharing, distribution and reproduction in any medium or format, as long as you give appropriate credit to the original author(s) and the source, provide a link to the Creative Commons licence, and indicate if you modified the licensed material. You do not have permission under this licence to share adapted material derived from this article or parts of it. The images or other third party material in this article are included in the article's Creative Commons licence, unless indicated otherwise in a credit line to the material. If material is not included in the article's Creative Commons licence and your intended use is not permitted by statutory regulation or exceeds the permitted use, you will need to obtain permission directly from the copyright holder. To view a copy of this licence, visit http://creativecommons.org/licenses/by-nc-nd/4.0/.

© The Author(s) 2026